CuS Nanodots with Ultrahigh Efficient Renal Clearance for Positron Emission Tomography Imaging and Image-Guided Photothermal Therapy

Min Zhou[†], **Junjie Li**[†], **Su Liang**[†], **Anil K. Sood**[‡,§], **Dong Liang**[⊥], and **Chun Li**[*,†,§]

[†]Department of Cancer Systems Imaging, The University of Texas MD Anderson Cancer Center, Houston, Texas 77030, United States

[‡]Departments of Gynecologic Oncology & Reproductive Medicine and Cancer Biology, The University of Texas MD Anderson Cancer Center, Houston, Texas 77030, United States

[§]Center for RNA Interference and Non-Coding RNA, The University of Texas MD Anderson Cancer Center, Houston, Texas 77030, United States

[⊥]Department of Pharmaceutical Sciences, Texas Southern University, Houston, Texas 77004, United States

Abstract

Translation of nanoparticles (NPs) into clinical practice has been limited by toxic effects induced by nonspecific accumulation of NPs in healthy organs after systemic administration. The ideal NPs should accumulate in the target site, carry out their function, and then ultimately be eliminated from the body. Here, we show a single-compartment, multifunctional ultrasmall copper sulfide nanodot (CuS ND) that is rapidly cleared from the body. These CuS NDs have a hydrodynamic diameter of <6 nm, can efficiently absorb near-infrared light for photothermal ablation therapy, and stably incorporate the copper-64 radioisotope for noninvasive positron emission tomography (PET). Importantly, ~95% of CuS NDs are excreted intact through the renal–urinary system within 24 h with minimal retention in the liver and the spleen. The ultrasmall CuS NDs accumulate in 4T1 tumors in Balb/c mice, as monitored by PET imaging, and mediate tumor ablation when combined with near-infrared light irradiation. As a first example of PET-visible, renal-clearable inorganic nanomaterials with peak absorption in the near-infrared region, CuS NDs represent a robust platform for cancer imaging and therapy.

Graphical abstract

[*]Address correspondence to cli@mdanderson.org.

Conflict of Interest: The authors declare no competing financial interest.
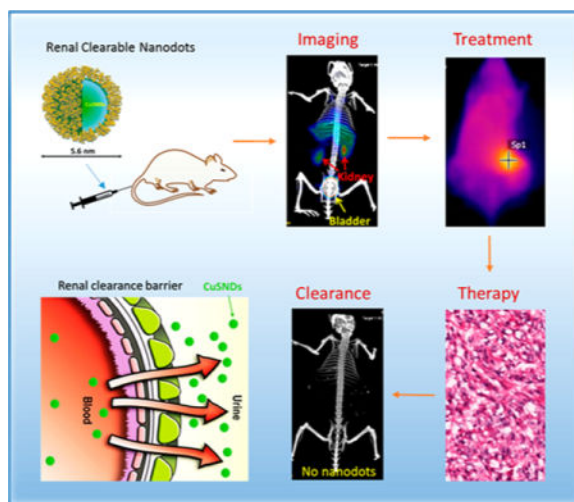
Keywords

renal clearance; CuS nanodots; photothermal therapy; PET imaging; toxicity

Nanoparticles (NPs) represent a promising technology for cancer detection and treatment owing to their unique physical and chemical properties.[1–3] However, the clinical use of NPs has been limited because most NPs possessing inherent physicochemical properties suitable for cancer diagnosis and therapy are non-degradable and can be retained in the body for a prolonged period.[4–6] NPs with a photothermal effect in the near-infrared (NIR) region (700–1100 nm wavelength) convert NIR light to heat, enabling deposition of otherwise benign optical energy into tumors for photothermal ablation (PTA) of tumor cells.[7–9] PTA therapy may also be used as an adjunct to conventional surgery, chemotherapy, radiotherapy, or immunotherapy.[10] Many NPs have been investigated for potential clinical application, including various gold nanostructures, such as gold nanoshells,[11,12] gold nanorods,[13,14] gold nanocages,[15,16] and hollow gold nanospheres,[17,18] carbon nanotubes,[19,20] graphene,[21,22] and copper-based NPs.[23–27] However, most of these NPs, which range from 10 to 200 nm in hydrodynamic diameter (HD), are eventually accumulated in the organs of the reticuloendothelial system (RES), such as the liver and spleen, and can be retained in the body for a prolonged period, which raises concerns about the long-term risk of adverse effects.[28–32] To date, photothermal conducting NPs with peak absorbance in the NIR region capable of rapid clearance from the body have not been available.

There are two different clearance routes for NPs after systemic administration: clearance *via* the liver (into bile) and clearance *via* the kidneys (into urine). Clearance *via* the renal–urinary route is desirable because of the rapidity of this process. Size and surface properties of NPs are important factors in influencing the route of clearance. NPs smaller than 6 nm in diameter can undergo renal clearance if surface charge is optimized for this pathway.[33] However, because of preparation methods or structural requirements for efficient photothermal effect with NIR light, such as structural anisotropy or core–shell structure for plasmonic metal nanomaterials, none of the NIR photothermal coupling agents reported to date are smaller than 6 nm. It has proven to be extremely challenging to develop a stable NP

platform that simultaneously satisfies the requirements for PTA therapy of solid tumors: high photothermal conversion efficiency, visibility on clinical imaging, and efficient body clearance. In this work, we have resolved these important problems and report a novel multifunctional, ultrasmall photothermal conversion agent, polyvinylpyrrolidone-coated CuS nanodots (CuS NDs), that has minimal nonspecific uptake in the RES organs and can be efficiently cleared from the body *via* the renal–urinary system. Nanoscale devices such as this may have broad preclinical and clinical implications.

RESULTS

Synthesis, Characterization, and Stability of CuS NDs

We developed a one-step synthesis process for CuS NDs, which requires a chemical reaction of Cu^{2+} ions with S^{2-} ions in the presence of polyvinylpyrrolidone (PVP). To synthesize CuS NDs with HD smaller than 6 nm, we systematically investigated the effect of the molecular weight and concentration of PVP on particle formation. We found that the size of PVP-coated CuS NPs was a function of the PVP molecular weight and concentration. By controlling these two variables, we were able to tune the HD of CuS NPs from a few nanometers to tens of nanometers (Supporting Information Table S1). PVP with a molecular weight of 10 kDa at a concentration of 100 mg/mL resulted in CuS NDs with an average HD of only 5.6 nm as measured with dynamic light scattering (DLS) in aqueous solution (Figure 1a). The average diameter of the corresponding NDs in the dry state as measured with high-resolution transmission electron microscopy was 4.3 nm (Figure 1b). X-ray photoelectron spectroscopy measurement of CuS NDs showed that the NDs were composed of copper and sulfur in a molar ratio of 49% copper to 51% sulfur. The corresponding N 1s, C 1s, and O 1s peaks were attributed to the surface coating of PVP (Supporting Information Figure S1). The surface charge of the NDs was almost neutral, as measured by ζ-potential analysis (Supporting Information Figure S2). Importantly, the 5.6 nm CuS NDs exhibited strong NIR absorption peaking at ~990 nm (Figure 1c). Exposure of a 2 OD (optical density = 100 μg/mL) CuS ND solution under continuous-wave NIR laser irradiation at 808 nm at a power density of 2 W/cm^2 for 10 min elevated the temperature of the solution from 23 to 50 °C (Figure 1d). Thus, the ultrasmall CuS NDs are an efficient photo-thermal coupling agent. These NDs could be lyophilized and resuspended in water, and such processing did not significantly change their optical absorption (Figure 1e).

Physiological stability of nanomaterials is critically important for their biomedical application. We measured the UV–vis spectra and DLS of the NDs after 5 day incubation in PBS (phosphate-buffered saline) and PBS containing 10% fetal bovine serum (FBS) at 37 °C. No particle aggregation could be visualized during the observation period. UV–vis analysis showed essentially no differences in the spectra and absorption intensities between baseline and 5 days of incubation in both media. DLS analysis showed almost no change in the HD of the NDs between baseline and 5 days of incubation (Supporting Information Figure S3). These findings indicated that CuS NDs were stable under these storage conditions.

Radiolabeling ^{64}Cu to CuS NDs

Radiolabeling with copper-64 (^{64}Cu) was achieved using procedures similar to those we previously reported for the synthesis of polyethylene glycol (PEG)-coated PEG-[^{64}Cu]CuS NPs.[23] The schematic structure of [^{64}Cu]CuS NDs is shown in Figure 1f. Here, the radio-isotope precursor, ^{64}CuCl$_2$, was the same element component as non-radio precursor CuCl$_2$; the ^{64}Cu was integrated to the as-prepared [^{64}Cu]CuS NDs homogeneously. Therefore, [^{64}Cu]CuS NDs showed extremely high radio-labeling efficiency. Radio thin-layer chromatography (radio-TLC) showed that more than 99% of radioactivity was associated with the [^{64}Cu]CuS NDs, which remained at the original spot with a retention factor of 0.0 (Figure 1g). After incubation in PBS and FBS solution at 37 °C for 2 days, more than 90% of radioactivities were associated with the NDs (Figure 1h and Supporting Information Figure S4).

Pharmacokinetics, Biodistribution, and PET/CT Imaging of CuS NDs

To investigate how the size of PVP-coated CuS NPs influenced their *in vivo* behavior, we compared the pharmacokinetics of 5.6 nm [^{64}Cu]CuS NDs and 19 nm [^{64}Cu]CuS NPs in female Swiss mice. The 19 nm [^{64}Cu]CuS NPs were synthesized according to conditions summarized in Supporting Information Table S1. As shown in Figure 2a, the blood activity–time course curves for both types of NPs after a single intravenous (i.v.) injection showed a biexponential disposition. Therefore, the pharmacokinetic parameters for each mouse were determined with a two-compartment model, and the mean and standard deviations of pharmacokinetic parameters are summarized in Table 1. Mean area under the blood concentration–time curve (AUC) for 19 nm NPs was significantly higher than that for the 5.6 nm NDs, indicating a lesser systemic exposure of the smaller NDs. Mean systemic clearance was significantly higher (over 3-fold) with 5.6 nm NDs, which also had larger volumes of distribution both in the central compartment (V1) and the peripheral compartment (V2). Mean terminal elimination half-life for 5.6 nm NDs was 11.69 h as opposed to 16.16 h for the 19 nm NPs. These data suggested that the 5.6 nm [^{64}Cu]CuS NDs behaved like small-molecular-weight compounds that can be cleared through the renal–urinary system.

Since rapid clearance from the blood may result from fast renal clearance and/or rapid removal by the RES, we compared the biodistribution of [^{64}Cu]CuS NPs of two different sizes in Swiss mice. As shown in Figure 2b, the 5.6 nm [^{64}Cu]CuS NDs had significantly lower uptake in most major organs at 24 h after i.v. injection. Notably, the liver uptake of the 5.6 nm [^{64}Cu]CuS NDs was only 15% of the uptake of the 19 nm [^{64}Cu]CuS NPs (4.29 ± 0.53 percentage of injected dose per gram of tissue [%ID/g] *vs* 28.13 ± 4.60%ID/g, $p < 0.0001$). The spleen uptake of the 5.6 nm [^{64}Cu]CuS NDs was only 24% of the uptake of the 19 nm [^{64}Cu]CuS NPs (0.97 ± 0.20%ID/g *vs* 4.15 ± 0.65%ID/g, $p < 0.001$).

MicroPET/CT (μPET/CT) images of Swiss mice acquired at different times after i.v. injection of 5.6 nm [^{64}Cu]CuS NDs are presented in Figure 2c. At 10 min after injection, the dominant PET signal was in the bladder and the kidney (Figure 2c,e,f). By 2 h after injection, the PET signal in the kidney was significantly decreased, indicating that the renal clearance of [^{64}Cu]CuS NDs occurred primarily during the first 2 h after NP injection. By 24 h after ND injection, PET signals were no longer discernible anywhere in the mice. The

residual radioactivity in the liver from [^{64}Cu]CuS NDs could be visualized only when the scale was readjusted to enhance image contrast (Supporting Information Figure S5. These data indicate that the majority of [^{64}Cu]CuS NDs were eliminated from the body by 24 h after injection. In contrast, at 10 min, 2 h, and 24 h after i.v. injection of the 19 nm CuS NPs, the majority of radioactivity remained in the liver (Figure 2d). Thus, particle size appears to be the primary factor accounting for evasion of the RES by CuS NDs.

Renal Clearance of CuS NDs

To examine whether the 5.6 nm [^{64}Cu]CuS NDs were retained in any of the remaining body parts not included in the biodistribution study, radioactivity present in the total mouse carcasses was measured. Quantitative analysis showed that more than 39.5% of the [^{64}Cu]CuS NDs were excreted from the body within 2 h and up to 95% within 24 h after i.v. injection (Figure 3a), indicating that [^{64}Cu]CuS NDs were efficiently eliminated from the body.

To obtain a better understanding of the mechanism of clearance *in vivo*, urine samples excreted from Swiss mice were collected at 2 h after i.v. injection of 5.6 nm [^{64}Cu]CuS NDs. The samples were analyzed by radio-TLC, DLS, and UV–vis spectroscopy (Figure 3). Radio-TLC showed only one spot (99.7% of total radioactivity) with a retention factor of 0.0, suggesting that no radioactive species were excreted into the urine in the form of free ^{64}Cu^{2+} ions or other soluble metabolites (Figure 3b). DLS measurement showed the presence of NDs with an average HD of 5.7 nm (Figure 3c), which was essentially the same as the HD for the freshly prepared NDs. Moreover, UV–vis analysis showed characteristic extinction spectra of [^{64}Cu]CuS NDs that peaked at ~990 nm (Figure 3d). TEM analysis of the urine sample collected at 2 h after injection showed NPs less than 5 nm in average diameter (Supporting Information Figure S6). Taken together, these data supported that [^{64}Cu]CuS NDs were excreted from the body in their intact form via the renal–urinary system.

In Vivo μPET/CT Imaging of CuS NDs in Tumor-Bearing Balb/c Mice

We next investigated the feasibility of using CuS NDs for in vivo tumor μPET/CT imaging. Figure 4a shows representative μPET/CT images of a Balb/c mouse with a 4T1 breast tumor acquired at 10 min, 2 h, and 24 h after i.v. injection of 5.6 nm [^{64}Cu]CuS NDs. Consistent with the PET imaging findings in the tumor-free Swiss mice, μPET/CT images revealed that most NDs were eliminated by renal clearance by 24 h. As expected, [^{64}Cu]CuS NDs initially accumulated in the tumor, permitting tumor visualization at 2 h after i.v. injection. Quantitative analysis showed that the tumor uptake of the NDs at 10 min, 2 h, and 24 h after ND injection was 1.69 ± 0.63, 3.62 ± 0.50, and 0.22 ± 0.04%ID/g, respectively; the average tumor-to-muscle ratios at those times were 4.11 ± 0.40, 10.74 ± 1.06, and 1.35 ± 0.16, respectively (Figure 4b).

In Vitro and *In Vivo* PTA Therapy of CuS NDs in a 4T1 Tumor Model

To test the cell killing induced by the photo-thermal effect through CuS NDs, 4T1 cells were incubated with CuS NDs for 2 h, washed, and then irradiated with an 808 nm NIR laser. At 24 h after laser treatment, cells treated with CuS NDs plus the NIR laser (2.0 W/cm^2 for 2

min) had substantially reduced cell density. No apparent change in cell viability was observed when cells were treated with CuS NDs alone or the NIR laser alone (Figure 5). These results demonstrated that CuS NDs mediated effective photothermal destruction of 4T1 cancer cells.

We next investigated the feasibility of using CuS NDs for PTA therapy *in vivo*. Because we observed the highest level of tumor uptake at 2 h after ND injection in the 4T1 model, laser treatment was delivered at 2 h after i.v. injection of CuS NDs (200 μL/mouse, 8 OD, 4 mg/kg, 100 μg/mouse). Upon laser treatment, the tumor surface temperature increased rapidly to reach 45.8 °C within 2 min (Figure 6a). Tumor temperature increased as a function of exposure time (Supporting Information Figure S7). In contrast, the tumor surface temperature was only 38.7 °C for saline-injected mice after the same exposure period (Figure 6a). Histological examination confirmed that i.v. injection of CuS NDs followed by laser irradiation 2 h later at a power density of 2.0 W/cm^2 for 2 min caused substantial damage to the tumor (Figure 6b). In this group of mice ($n = 3$), more than 95% of tumor tissue was necrotized. Common features of thermo-necrosis were found in the tumor tissues, such as loss of nucleus, cell shrinkage, and coagulation. Few viable cells were found within the tumor tissue. In contrast, in the mice treated with saline or saline plus laser, there was only a baseline fraction of necrosis in tumor tissue (<3%) (Figure 6c). Tumor necrosis was significantly greater in mice treated with CuS NDs plus laser than in mice treated with saline alone or saline plus laser ($p < 0.001$). These findings indicated that CuS NDs are capable of mediating effective photothermal destruction of solid tumors *in vivo*.

We next carried out an *in vivo* tumor growth study on the 4T1 orthotopic tumor model. Four groups of 4T1 tumor-bearing mice with five mice per group were used in this experiment. Saline or CuS ND solutions (200 μL/mouse, 8 OD, 4 mg/kg) were i.v. injected into these mice. The tumors were irradiated by the 808 nm laser at the power density of 2.0 W/cm^2 for 2 min at 2 h postinjection. The tumor sizes were then measured by a caliper every 2–3 days. The tumors in all three control groups showed similar growth rate, suggesting that neither laser irradiation of tumors nor CuS NDs alone affected the tumor growth. Remarkably, tumors on mice treated with CuS NDs plus NIR laser irradiation were completely eliminated post-treatment (Figure 7). Our results demonstrate the excellent therapeutic effect of the CuS ND-mediated PTA.

Pilot Toxicity Study

PVP is known to be nontoxic and has been used in a wide variety of pharmaceutical applications, such as in tablets; oral solutions, syrups, and drops; injectable and topical solutions; and film coatings on tablets. To evaluate the potential toxicity of PVP-coated CuS NDs, we tested the toxicity of PVP-CuS NPs *in vitro* and *in vivo*. *In vitro*, CuS NDs demonstrated relatively low cytotoxicity against both human embryonic kidney 293 cells (HEK-293, representing kidney cells) and human hepatocellular carcinoma HepG2 cells (representing hepatocytes) (Supporting Information Figure S8a,b). The inhibitory concentration at the 50% level (IC$_{50}$) after 24 h incubation was estimated to be 66 OD (3.3 mg/mL) for HEK-293 cells and 49 (2.45 mg/mL) OD for HepG2 cells; after 72 h incubation, the IC$_{50}$ values were estimated to be 7 OD (0.35 mg/mL) for HEK-293 cells and 18 OD (0.9

mg/mL) for HepG2 cells. An initial dose-finding toxicity study showed that, in CD1 mice, a single i.v. dosing of 120 OD CuS NDs (0.2 mL/mouse, equivalent dose 60 mg/kg for mouse weighing 20 g) did not cause any death in the tested mice and no apparent toxic effects were noted during a 20 day observation period. CuS NPs at this dose did not cause significant body weight change (Supporting Information Figure S8c). In addition, blood biochemistry and hematology analysis was performed on male CD1 mice 24 h after i.v. injection of CuS NDs at doses of 4 mg/kg (8 OD), 40 mg/kg (80 OD), and 80 mg/kg (160 OD). Creatinine levels in mice 24 h after i.v. injection of CuS NDs in all treatment groups were less than 0.20 mg/dL. No significant changes in blood biochemistry and hematology parameters with $p <$ 0.01 were detected, indicating normal liver and kidney functions and normal blood clotting and blood chemistry (Figure 8). Therefore, CuS NDs appeared to be a rather safe agent to the treated mice even at a very high dose.

DISCUSSION

In this work, we report a novel multifunctional, ultrasmall photothermal conversion agent, PVP-coated CuS NDs, that can be efficiently cleared from the body *via* the renal–urinary system. We found that CuS NDs displayed peak absorption at 990 nm and that ~95% of the particles were eliminated within 24 h after i.v. injection. Other studies have reported efficient renal clearance of quantum dots,[34–37] iron oxide NPs,[38] tantalum oxide NPs,[39] zwitterionic-coated stealth NPs,[40] and ultrasmall Au nanoparticles.[41–43] These studies indicate that particle size and surface charge are the primary factors accounting for evasion of the RES and efficient renal clearance. The size of our CuS NDs is smaller than 6 nm, which is below the glomerular capillary filtration size threshold (6 nm).[5,33] The PVP-coated CuS NDs also displayed an almost neutral surface charge. These factors may have contributed to the efficient renal clearance of the 5.6 nm CuS NDs.

Another factor that may have contributed to the efficient renal clearance of the 5.6 nm CuS NDs is low serum protein adsorption onto these NPs. Although NPs smaller than the kidney filtration threshold (~6 nm) are expected to pass through the kidney filtration barrier, some ultrasmall NPs (HD < 6 nm) are still not renal-clearable and are sequestered by RES organs. For instance, only 9%ID of 1.4 nm gold NPs coated with bis(*p*-sulfonatophenyl)phenylphosphine could be excreted into urine and >50%ID of the NPs were found in the liver 24 h after i.v. injection.[44] Furthermore, 4 nm quantum dots coated with anionic dihydrolipoic acid or cationic cysteamine were not renal-clearable and mainly accumulated in the liver, lung, and spleen.[37] The reason for such high accumulation of these ultrasmall NPs in RES organs is thought to be protein adsorption induced by the surface ligands on the NPs. Like PEG, PVP is a neutral hydrophilic polymer. Introducing PVP onto the NP surface can significantly decrease protein adsorption and improve blood compatibility.[45–47] Indeed, we found that CuS NDs displayed a level of protein absorption significantly lower than that of both citrate-coated CuS NPs and PEG-CuS NPs (Supporting Information Figure S9).

Our data also confirm that particle size is an important property for evasion of the RES. The 5.6 nm CuS NDs displayed only 15% of the liver uptake and 24% of the spleen uptake observed with the corresponding 19 nm CuS NPs. Furthermore, although PEG is considered

to be one of the best coating materials that help NPs evade the RES, the 5.6 nm CuS NDs displayed substantially less liver and spleen uptake than the 32 nm PEG-CuS NPs did.[23] A small amount of [^{64}Cu]CuS NDs was deposited in the liver, probably because of the presence of a small fraction of nanoparticles with a HD of greater than 6 nm (Figure 2b and Supporting Information Figure S5). Future work to produce CuS NDs with narrower size distribution is expected to further reduce the uptakes of these multifunctional NDs in the liver.

Nanomaterials that could be cleared from the body may overcome one of the major concerns associated with the clinical translation of functional NPs, that is, toxic effects due to nonspecific accumulation of NPs in healthy organs. Initial dose finding toxicity study showed that no death of mice had occurred at an injected dose of up to 60 mg/kg. This dose was 15 times greater than the effective dose used in the *in vivo* PTA of 4T1 tumors. Preliminary acute blood biochemistry and hematology studies showed that treatment with CuS NDs at doses up to 80 mg/kg did not affect liver function, kidney functions, and blood chemistry (Figure 8).

To ensure the safety and efficacy of PTA therapy, one must be able to correlate tissue damage with the amount of NPs accumulated in the target tissue. Thus, noninvasive quantitation of tissue concentration NPs is important for pretreatment planning and monitoring of response to therapy. By introducing a positron emitter ^{64}Cu to the synthesis, we enabled noninvasive imaging of our renal-clearable NPs with the clinically available imaging technique PET, which is a quantitative, highly sensitive modality capable of deep-tissue imaging.[48,49] Using both PET imaging and the cut-and-count method, we found that [^{64}Cu]CuS NDs accumulated in solid tumors, possibly through the "enhanced permeability and retention" effect. This was sufficient to mediate an effective photothermal ablation therapeutic effect (Figures 6 and 7).

CONCLUSIONS

In conclusion, we report CuS NDs as a renal-clearable nanoparticle system for image-guided photothermal therapy. Compared to larger-sized nanomaterials, the ultrasmall 5.6 nm CuS NDs can pass through the barrier for efficient renal clearance, minimizing the RES adsorption, but demonstrate strong absorption in the near-infrared region. Due to their efficiently renal-clearable, PET-visible, and excellent NIR light-activatable properties, the CuS NDs may have broad preclinical and clinical implications. While our work reported here represents important steps toward achieving the desired properties of NPs for clinical application, such as efficient passive targeting and renal clearance, long-term *in vivo* toxicity should be explored in the near future. Moreover, the tumor uptake of the current CuS NDs still has room for improvement. The standard approach to improve the tumor uptake of NPs is to introduce receptor-specific targeting moieties; however, introducing targeting moieties to ultrasmall CuS NDs eventually increases their overall HD, and this may prevent their renal clearance. Therefore, a balance must be struck between adding target moieties, which increases the size of the NPs, and keeping the diameter of the NPs small enough to allow renal clearance and prevent undesired nonspecific background retention. These important trade-offs should be explored in future studies.

EXPERIMENTAL SECTION

Materials

Copper(II) chloride ($CuCl_2$), sodium sulfide ($Na_2S \cdot 9H_2O$), sodium citrate, polyvinylpyrrolidone (PVP) K15 (molecular weight = 10 000 Da), PVP K30 (molecular weight = 40 000 Da), PVP K90 (molecular weight = 360 000 Da), and methoxy–PEG–thiol (molecular weight = 5000 Da) were purchased from Sigma-Aldrich (St. Louis, MO). Isoflurane was purchased from Baxter (Deerfield, IL). $^{64}CuCl_2$ was supplied by the Cyclotron Radiochemistry Facility at The University of Texas MD Anderson Cancer Center (Houston, TX). All the chemicals and solvents were at least American Chemical Society grade and were used without further purification. Deionized water (18 MΩ) was obtained using a Milli-Q synthesis system (Millipore, Billerica, MA). 4T1 cells were obtained from American Type Culture Collection (Manassas, VA). RPMI-1640 culture medium, calcein AM, and ethidium homodimer-1 were obtained from Sigma-Aldrich.

General Procedures for the Synthesis of CuS NDs

Into 100 mL of aqueous solution containing $CuCl_2$ (1 mM) and PVP of preselected molecular weight and concentration was added 0.1 mL of Na_2S solution (1 M) under stirring at room temperature. For the synthesis of 5.6 nm NPs, PVP with a molecular weight of 10 kDa at a concentration of 100 mg/mL was used. For the synthesis of 19 nm NPs, PVP with a molecular weight of 40 kDa at a concentration of 3 mg/mL was used (Supporting Information Table S1). Beginning 5 min after mixing, the reaction mixture was heated to 90 °C and stirred for 15 min until a dark green solution was obtained. The solution was then transferred to ice-cold water. The resulting CuS NDs were purified by ultracentrifugation using an Amicon Ultra-15 centrifugal filter unit (Millipore) and stored at 4 °C. The NP size was tunable by adjustment of the molecular weight and concentration of PVP without a size selection process.

General Procedures for the Synthesis of Radioactive [^{64}Cu]CuS NPs

For the synthesis of 5.6 nm [^{64}Cu]CuS NDs, $^{64}CuCl_2$ (10 μL, 37 MBq) was added to 1 mL of $CuCl_2$ solution (1 mM) containing PVP (100 mg/mL, molecular weight 10 kDa). Then, 1 μL of Na_2S solution (1 M) was added to the $^{64}CuCl_2$/$CuCl_2$ solution under stirring at room temperature. Similar procedures followed those used for the synthesis of cold CuS NDs. The 19 nm [^{64}Cu]CuS NPs were similarly synthesized using PVP with a molecular weight of 40 kDa at a concentration of 3 mg/mL. The radiolabeling efficiency and the stability of radioactive NPs were analyzed using instant TLC. The instant TLC strips were developed with PBS (pH 7.4) containing 4 mM ethylenediaminetetraacetic acid (EDTA), and radioactivity was quantified using a Bioscan IAR-2000 TLC imaging scanner (Washington, DC). For the study of labeling stability, [^{64}Cu]CuS ND solution in PBS or PBS containing 10% FBS was incubated at 37 °C for 48 h. The radioactivity at the original spot was recorded as a percentage of the total radioactivity of the ITLC strip.

Characterization of CuS NPs

A PHI Quantera SXM XPS/ESCA system (Ulvac-PHI, INC, Japan) at 5×10^{-9} Torr was used to take X-ray photoelectron spectra. A monochromatic Al X-ray source at 100 W was used with an analytical spot size of 0.15 mm × 1.4 mm and a 45° takeoff angle, with a pass energy of 26.00 eV. For transmission electron microscopy, an aqueous solution of CuS NPs was deposited on carbon-enhanced copper grids without negative staining. The NPs were allowed to adhere on the grid for 1 h, after which they were briefly rinsed with deionized water and air-dried. The samples were then examined using a transmission electron microscope (JEM 2010, JEOL Japan) at an accelerating voltage of 200 kV. Digital images were obtained using the AMT imaging system (Advanced Microscopy Techniques Corp., Danvers, MA). UV–vis spectroscopy of CuS NPs was performed with a Beckman Coulter DU-800 UV–vis spectrometer (Brea, CA) with a 1.0 cm optical path length quartz cuvette. For stability testing, solutions of 5.6 nm CuS NDs in PBS or PBS containing 10% FBS were stored at 37 °C for 5 days. Aliquots were taken at day 1 and day 5 for DLS size measurement and UV–vis spectrum recording. No precipitation was observed by visual inspection. For quantification of protein absorption, aqueous solutions of CuS NDs, PEG-CuS NPs, and citrate-coated CuS NPs (Cit-CuS NPs) (0.4 mg/mL) were incubated with an aqueous solution of human serum albumin (HSA, 50 μg/mL) at room temperature for 3 days. After ultracentrifugation, the unabsorbed protein in the filtrate was quantified directly using UV–vis spectrometry at 277 nm. The absorbed protein was expressed as percentage of concentration change in the filtrate to the original HSA concentration.

Photothermal Effect in Aqueous Solution

The NIR laser system used in this study consisted of a commercially available 808 nm diode laser (PhoTex15; Visualase, Inc., Houston, TX) and a 5 m, 600 μm core BioTex LCM-001 optical fiber (BioTex Inc., Houston, TX) used to transfer laser power from the laser unit to the target. This fiber had a lens mounting at the output that allowed the laser spot size to be changed by changing the distance from the output to the target. For measurement of temperature change mediated by CuS NDs, NIR laser light (2.0 W/cm^2, spot size 10 mm in diameter) was delivered through a quartz cuvette containing the CuS NDs (0.1 mg/mL, 200 μL). A thermocouple was inserted into the aqueous solution of NDs perpendicular to the path of the laser light. The temperature was measured over 10 min. Thermographic pictures were taken using a thermal camera (Flir i7, Flir Systems, Inc., Portland, OR).

Cytotoxicity

Cell viability after CuS ND treatment was analyzed by using the MTS assay. Briefly, cells were maintained in DMEM containing 10% FBS and 0.2% normocin at 37 °C in a humidified atmosphere with 5% CO$_2$. Cells were seeded in a 96-well flat bottom plate at a density of 1×10^4 cells/well for at least 24 h prior to treatment. Cells were treated with different concentration of the CuS NDs (suspended in normal water and diluted in DMEM, 100 μL per well), five wells per concentration. After 24 or 72 h of treatment, the cells were washed with PBS followed by the addition of 100 μL of MTS in phenol-free media solution (1:5 ratio) and were incubated for an additional 4 h at 37 °C. Absorbance at 490 nm was measured against a background control using a BioTek Instrument microplate reader. Data

were reported as mean ± standard deviation. Wells treated with media represent 100% viable cells, and wells containing no cells represent background signal. The viability data were analyzed in GraphPad Prism.

Animals and Tumor Models

Animal protocols were approved by the Institutional Animal Care and Use Committee. Female Swiss mice and Balb/c mice, aged 8–12 weeks, were purchased from Taconic Biosciences Inc. (Hudson, NY). To obtain the breast tumor model, 1×10^6 viable 4T1 tumor cells suspended in PBS were injected subcutaneously to right thigh (for μPET/CT study) or orthotopically to mammary fat pad (for PTA study) of each Balb/c mouse.

Pharmacokinetics

For the pharmacokinetic study, female Swiss mice (8 weeks) were injected intravenously with radioactive CuS NPs (1.85 MBq/mouse in 0.2 mL), and blood samples (10 μL) were collected from the tail vein at predetermined time points. The blood pharmacokinetic parameters of the radio-tracer were analyzed with Phoenix 1.3 (Certara, St. Louis, MO). The plasma concentration *versus* time curves were generated by SigmaPlot 12.3 (Systat Software, San Jose, CA). The animals were euthanized by CO_2 exposure at the end of the study. All pharmacokinetic analyses were made using classical techniques and the microcomputer-based program Phoenix WinNonlin 6.3 software (Pharsight Corp., St. Louis, MO). Model selection was based on the Akaike Information Criterion (AIC) and analysis of the weighted residuals. The following two-compartmental model optimally fitted individual concentration *versus* time data from each mouse:

$$Ct = A \cdot e - \alpha t + B \cdot e - \beta t$$

where Ct is the blood concentration at time t, α is the distribution rate constant, β is the terminal elimination rate constant, and A and B are intercept parameters. Systemic clearance (CL), volume of distributions in center compartment (V_1), and peripheral compartment (V_2) as well as mean resident time (MRT) were also estimated. Area under the blood concentration–time curve from zero to infinity was estimated using the trapezoidal rule and linear extrapolation to infinite time. Mean pharmacokinetic parameters between nanoparticle groups were statistically compared using the unpaired Student's *t* test.

For estimation of whole body retention of nanoparticles, female Swiss mice were injected with 5.6 nm [^{64}Cu]CuS NDs or 32 nm [^{64}Cu]CuS NPs (n = 3). The whole body radioactivity was measured using a radioactivity dose calibrator (CRC-25W, Capintec Inc., Ramsey, NJ) at different times after injection. All the mice were anesthetized before the measurement. Percentage of excreted radioactivity at different times after i.v. injection of 5.6 nm [^{64}Cu]CuS NDs was then calculated by subtracting the remaining radioactivity in the whole animal from the total injected radioactivity measured by counting radioactivity of the whole animal immediately after injection.

Biodistribution

Normal female Swiss mice were used to study biodistribution. Swiss mice were divided into two groups; mice in one group were injected with 19 nm [^{64}Cu]CuS NPs, and mice in the second group were injected with 5.6 nm [^{64}Cu]CuS NDs. In each mouse, NPs were injected intravenously in 0.2 mL of saline at a dose of 0.74 MBq per mouse. Mice were killed by CO_2 overexposure 24 h after NP injection. Blood, heart, liver, spleen, kidney, lung, stomach, intestine, muscle, bone, brain, and tumor tissues were removed and weighed, and radioactivity was measured with a Packard Cobra gamma counter (Ramsey, MN). Uptake of ^{64}Cu-labeled CuS NPs in various organs was expressed as %ID/g.

μPET/CT Imaging

Normal Swiss mice and Balb/c mice bearing subcutaneous 4T1 tumors (tumor diameter =~ 5 × 7 mm) were used for the μPET imaging studies. Mice in each group ($n = 3$) were injected intravenously with [^{64}Cu]CuS NDs (7.4 MBq/mouse; 0.2 mL). The animals were anesthetized with 2% isoflurane and placed in the prone position, and μPET/CT images were acquired at 10 min, 2–4 h, and 24 h after NP injection using an Inveon μPET/CT scanner (Siemens Preclinical Solutions, Knoxville, TN). The image requisition time was 5 min. The μPET and CT images were generated separately and then fused. PET images were co-registered to CT using a preset transformation matrix using Inveon Research Workplace (Siemens Preclinical Solution). For data analysis, the region of interest was manually drawn covering the whole tumor on CT images and copied to the corresponding PET images. Similarly, a circular region of interest was drawn on the muscle of the opposite leg of the mouse on CT images and copied to the PET images. The mean signal intensities of the tumor, liver, bladder, kidney, and muscle in the regions of interest were recorded.

PTA of Cancer Cells with CuS NDs *in Vitro*

4T1 cells were seeded onto a 96-well plate with a density of 10 000 cells per well 1 day before the experiment. Cells were washed three times with Hanks balanced salt solution (Sigma-Aldrich) and then incubated with CuS NDs in RPMI-1640 culture medium at a concentration of 4 OD (0.2 mg/mL) at 37 °C. Cells without NPs were used as a control. Two hours later, the culture medium was replaced with fresh RPMI-1640 medium without phenol red, and the cells were irradiated with a diode NIR laser centered at 808 nm at an output power of 2 W/cm^2 for 2 min. After treatment, cells were resupplied with RPMI-1640 medium containing 10% FBS. Twenty-four hours later, the cells were washed with Hanks balanced salt solution and stained with calcein AM dye, which reports ubiquitous intracellular esterase activity, and ethidium homodimer-1, which is a cell-impermeable stain that emits red fluorescence when bound to DNA (Invitrogen). The cell viability after exposure to the NIR laser was evaluated using under a Zeiss Axio Observer.Z1 fluorescence microscope (Carl Zeiss MicroImaging GmbH, Göttingen, Germany).

PTA of Cancer Cells with CuS NDs *in Vivo*

Balb/c mice bearing a 4T1 tumor (average tumor diameter = ~ 3–6 mm, 7 days after inoculation) in the mammary fat pads were randomly allocated into four groups ($n = 3$). Mice in groups A and C were injected intravenously with saline. Mice in groups B and D

were injected intravenously with CuS NDs (8 OD, 4 mg/kg, 100 μg/mouse). Two hours later, the tumors in mice from groups C and D were irradiated with an 808 nm NIR laser at 2 W/cm^2 for 2 min. Thermographic pictures were taken using a thermal camera. The mice were killed 24 h after laser treatment, and tumors were removed, snap-frozen, and cryosectioned into 20 μm thick sections. One histological section was obtained from each tumor specimen and stained with hematoxylin and eosin. The sections were examined under a Zeiss Axio Observer.Z1 fluorescence microscope. The extent of tumor necrosis, expressed as a percentage of the entire tumor area, was analyzed with Zeiss AxioVision software (version 4.6.3).

For tumor growth delay study, Balb/c mice bearing a 4T1 tumor (tumor diameter = ~2–5 mm, 5 days after inoculation) in the mammary fat pads were randomly allocated into four groups ($n = 5$). Mice in groups A and C were injected intravenously with saline. Mice in groups B and D were injected intravenously with CuS NDs (8 OD, 4 mg/kg, 100 μg/mouse). Two hours later, the tumors in mice from groups C and D were irradiated with an 808 nm NIR laser at 2 W/cm^2 for 2 min. After treatments, the length and width of the tumors were monitored by a digital caliper every 2–3 days for 17 days. The tumor volume was calculated according to the following formula: width^2 × length/2.

Pilot Toxicity Study

Toxicity experiments were carried out with 8 week old male CD1 mice. Mice were injected through the tail vein with CuS NDs (8, 80, or 160 OD; 0.2 mL/mouse; equivalent doses of 4, 40, or 80 mg/kg) or an equal volume of PBS ($n = 5$–6/group). Twenty-four hours later, mice were killed after cardiac puncture to obtain blood for hematologic and clinical chemistry analysis. For body weight measurement, each male CD1 mouse ($n = 6$) received a single i.v. injection of CuS NDs (0.2 mL/mouse) at a concentration of 120 OD (equivalent dose of 60 mg/kg).

Statistical Analysis

Differences in pharmacokinetic, biodistribution, and necrosis (expressed as percentage of necrotic area) were analyzed using the two-tailed Student's t test. Differences between groups were considered statistically significant at $p < 0.05$.

Supplementary Material

Refer to Web version on PubMed Central for supplementary material.

Acknowledgments

REFERENCES AND NOTES

1. Service RF. Nanotechnology Takes Aim at Cancer. Science. 2005; 310:1132–1134. [PubMed: 16293748]

2. Davis ME, Chen Z, Shin DM. Nanoparticle Therapeutics: An Emerging Treatment Modality for Cancer. Nat Rev Drug Discovery. 2008; 7:771–782. [PubMed: 18758474]

3. Thakor AS, Gambhir SS. Nanooncology: The Future of Cancer Diagnosis and Therapy. Ca-Cancer J Clin. 2013; 63:395–418. [PubMed: 24114523]

4. Li C. A Targeted Approach to Cancer Imaging and Therapy. Nat Mater. 2014; 13:110–115. [PubMed: 24452345]

5. Liu JB, Yu MX, Zhou C, Zheng J. Renal Clearable Inorganic Nanoparticles: A New Frontier of Bionanotechnology. Mater Today. 2013; 16:477–486.

6. Scheinberg DA, Villa CH, Escorcia FE, McDevitt MR. Conscripts of the Infinite Armada: Systemic Cancer Therapy Using Nanomaterials. Nat Rev Clin Oncol. 2010; 7:266–276. [PubMed: 20351700]

7. Melancon MP, Zhou M, Li C. Cancer Theranostics with Near-Infrared Light-Activatable Multimodal Nanoparticles. Acc Chem Res. 2011; 44:947–956. [PubMed: 21848277]

8. Shanmugam V, Selvakumar S, Yeh CS. Near-Infrared Light-Responsive Nanomaterials in Cancer Therapeutics. Chem Soc Rev. 2014; 43:6254–6287. [PubMed: 24811160]

9. Liang C, Wang C, Feng L, Yang K, Liu Z. Functional Nanomaterials for Phototherapies of Cancer. Chem Rev. 2014; 114:10869–10939. [PubMed: 25260098]

10. Chu KF, Dupuy DE. Thermal Ablation of Tumours: Biological Mechanisms and Advances in Therapy. Nat Rev Cancer. 2014; 14:199–208. [PubMed: 24561446]

11. Hirsch LR, Stafford RJ, Bankson JA, Sershen SR, Rivera B, Price RE, Hazle JD, Halas NJ, West JL. Nanoshell-Mediated Near-Infrared Thermal Therapy of Tumors under Magnetic Resonance Guidance. Proc Natl Acad Sci USA. 2003; 100:13549–13554. [PubMed: 14597719]

12. Melancon MP, Lu W, Zhong M, Zhou M, Liang G, Elliott AM, Hazle JD, Myers JN, Li C, Stafford RJ. Targeted Multifunctional Gold-Based Nanoshells for Magnetic Resonance-Guided Laser Ablation of Head and Neck Cancer. Biomaterials. 2011; 32:7600–7608. [PubMed: 21745689]

13. Huang X, El-Sayed IH, Qian W, El-Sayed MA. Cancer Cell Imaging and Photothermal Therapy in the Near-Infrared Region by Using Gold Nanorods. J Am Chem Soc. 2006; 128:2115–2120. [PubMed: 16464114]

14. Huang X, El-Sayed I, El-Sayed MA. Applications of Gold Nanorods for Cancer Imaging and Photothermal Therapy. Methods Mol Biol. 2010; 624:343–357. [PubMed: 20217607]

15. Chen JY, Wang DL, Xi JF, Au L, Siekkinen A, Warsen A, Li ZY, Zhang H, Xia YN, Li XD. Immuno Gold Nanocages with Tailored Optical Properties for Targeted Photothermal Destruction of Cancer Cells. Nano Lett. 2007; 7:1318–1322. [PubMed: 17430005]

16. Chen JY, Glaus C, Laforest R, Zhang Q, Yang MX, Gidding M, Welch MJ, Xia YN. Gold Nanocages as Photothermal Transducers for Cancer Treatment. Small. 2010; 6:811–817. [PubMed: 20225187]

17. You J, Zhang R, Xiong C, Zhong M, Melancon M, Gupta S, Nick AM, Sood AK, Li C. Effective Photothermal Chemotherapy Using Doxorubicin-Loaded Gold Nanospheres That Target Ephb4 Receptors in Tumors. Cancer Res. 2012; 72:4777–4786. [PubMed: 22865457]

18. Zhao N, You J, Zeng Z, Li C, Zu Y. An Ultra pH-Sensitive and Aptamer-Equipped Nanoscale Drug-Delivery System for Selective Killing of Tumor Cells. Small. 2013; 9:3477–3484. [PubMed: 23609964]

19. Chakravarty P, Marches R, Zimmerman NS, Swafford ADE, Bajaj P, Musselman IH, Pantano P, Draper RK, Vitetta ES. Thermal Ablation of Tumor Cells with Antibody-Functionalized Single-Walled Carbon Nanotubes. Proc Natl Acad Sci USA. 2008; 105:8697–8702. [PubMed: 18559847]

20. Moon HK, Lee SH, Choi HC. *In Vivo* Near-Infrared Mediated Tumor Destruction by Photothermal Effect of Carbon Nanotubes. ACS Nano. 2009; 3:3707–3713. [PubMed: 19877694]

21. Yang K, Zhang S, Zhang G, Sun X, Lee S-T, Liu Z. Graphene in Mice: Ultrahigh *In Vivo* Tumor Uptake and Efficient Photothermal Therapy. Nano Lett. 2010; 10:3318–3323. [PubMed: 20684528]

22. Robinson JT, Tabakman SM, Liang YY, Wang HL, Casalongue HS, Vinh D, Dai HJ. Ultrasmall Reduced Graphene Oxide with High Near-Infrared Absorbance for Photothermal Therapy. J Am Chem Soc. 2011; 133:6825–6831. [PubMed: 21476500]

23. Zhou M, Zhang R, Huang M, Lu W, Song S, Melancon MP, Tian M, Liang D, Li C. A Chelator-Free Multifunctional [^{64}Cu]CuS Nanoparticle Platform for Simultaneous Micro-PET/CT Imaging

and Photothermal Ablation Therapy. J Am Chem Soc. 2010; 132:15351–15358. [PubMed: 20942456]

24. Ramadan S, Guo LR, Li YJ, Yan BF, Lu W. Hollow Copper Sulfide Nanoparticle-Mediated Transdermal Drug Delivery. Small. 2012; 8:3143–3150. [PubMed: 22829400]

25. Hessel CM, Pattani VP, Rasch M, Panthani MG, Koo B, Tunnell JW, Korgel BA. Copper Selenide Nanocrystals for Photothermal Therapy. Nano Lett. 2011; 11:2560–2566. [PubMed: 21553924]

26. Tian QW, Tang MH, Sun YG, Zou RJ, Chen ZG, Zhu MF, Yang SP, Wang JL, Wang JH, Hu JQ. Hydrophilic Flower-like CuS Superstructures as an Efficient 980 nm Laser-Driven Photothermal Agent for Ablation of Cancer Cells. Adv Mater. 2011; 23:3542–3547. [PubMed: 21735487]

27. Zhou M, Ku G, Pageon L, Li C. Theranostic Probe for Simultaneous *In Vivo* Photoacoustic Imaging and Confined Photothermolysis by Pulsed Laser at 1064 nm in 4T1 Breast Cancer Model. Nanoscale. 2014; 6:15228–15235. [PubMed: 25379880]

28. Schipper ML, Iyer G, Koh AL, Cheng Z, Ebenstein Y, Aharoni A, Keren S, Bentolila LA, Li J, Rao J, et al. Particle Size, Surface Coating, and PEGylation Influence the Biodistribution of Quantum Dots in Living Mice. Small. 2009; 5:126–134. [PubMed: 19051182]

29. Jokerst JV, Lobovkina T, Zare RN, Gambhir SS. Nanoparticle PEGylation for Imaging and Therapy. Nanomedicine. 2011; 6:715–728. [PubMed: 21718180]

30. You J, Zhou J, Zhou M, Liu Y, Robertson JD, Liang D, Van Pelt C, Li C. Pharmacokinetics, Clearance, and Biosafety of Polyethylene Glycol-Coated Hollow Gold Nanospheres. Part Fibre Toxicol. 2014; 11:26. [PubMed: 24886070]

31. Liu Z, Cai W, He L, Nakayama N, Chen K, Sun X, Chen X, Dai H. *In Vivo* Biodistribution and Highly Efficient Tumour Targeting of Carbon Nanotubes in Mice. Nat Nanotechnol. 2007; 2:47–52. [PubMed: 18654207]

32. Yang ST, Guo W, Lin Y, Deng XY, Wang HF, Sun HF, Liu HF, Wang X, Wang W, Chen M, et al. Biodistribution of Pristine Single-Walled Carbon Nanotubes *in Vivo*. J Phys Chem C. 2007; 111:17761–17764.

33. Longmire M, Choyke PL, Kobayashi H. Clearance Properties of Nano-Sized Particles and Molecules as Imaging Agents: Considerations and Caveats. Nanomedicine. 2008; 3:703–717. [PubMed: 18817471]

34. Choi HS, Gibbs SL, Lee JH, Kim SH, Ashitate Y, Liu FB, Hyun H, Park G, Xie Y, Bae S, et al. Targeted Zwitterionic Near-Infrared Fluorophores for Improved Optical Imaging. Nat Biotechnol. 2013; 31:148–153. [PubMed: 23292608]

35. Choi HS, Liu WH, Liu FB, Nasr K, Misra P, Bawendi MG, Frangioni JV. Design Considerations for Tumour-Targeted Nanoparticles. Nat Nanotechnol. 2010; 5:42–47. [PubMed: 19893516]

36. Choi HS, Ipe BI, Misra P, Lee JH, Bawendi MG, Frangioni JV. Tissue- and Organ-Selective Biodistribution of NIR Fluorescent Quantum Dots. Nano Lett. 2009; 9:2354–2359. [PubMed: 19422261]

37. Choi HS, Liu W, Misra P, Tanaka E, Zimmer JP, Ipe BI, Bawendi MG, Frangioni JV. Renal Clearance of Quantum Dots. Nat Biotechnol. 2007; 25:1165–1170. [PubMed: 17891134]

38. Zhou ZJ, Wang LR, Chi XQ, Bao JF, Yang LJ, Zhao WX, Chen Z, Wang XM, Chen XY, Gao JH. Engineered Iron-Oxide-Based Nanoparticles as Enhanced T-1 Contrast Agents for Efficient Tumor Imaging. ACS Nano. 2013; 7:3287–3296. [PubMed: 23473444]

39. Bonitatibus PJ, Torres AS, Kandapallil B, Lee BD, Goddard GD, Colborn RE, Marino ME. Preclinical Assessment of a Zwitterionic Tantalum Oxide Nanoparticle X-ray Contrast Agent. ACS Nano. 2012; 6:6650–6658. [PubMed: 22768795]

40. Garcia KP, Zarschler K, Barbaro L, Barreto JA, O'Malley W, Spiccia L, Stephan H, Graham B. Zwitterionic-Coated "Stealth" Nanoparticles for Biomedical Applications: Recent Advances in Countering Biomolecular Corona Formation and Uptake by the Mononuclear Phagocyte System. Small. 2014; 10:2516–2529. [PubMed: 24687857]

41. Liu JB, Yu MX, Ning XH, Zhou C, Yang SY, Zheng J. PEGylation and Zwitterionization: Pros and Cons in the Renal Clearance and Tumor Targeting of Near-IR-Emitting Gold Nanoparticles. Angew Chem, Int Ed. 2013; 52:12572–12576.

42. Zhou C, Long M, Qin YP, Sun XK, Zheng J. Luminescent Gold Nanoparticles with Efficient Renal Clearance. Angew Chem, Int Ed. 2011; 50:3168–3172.

43. Liu JB, Yu MX, Zhou C, Yang SY, Ning XH, Zheng J. Passive Tumor Targeting of Renal-Clearable Luminescent Gold Nanoparticles: Long Tumor Retention and Fast Normal Tissue Clearance. J Am Chem Soc. 2013; 135:4978–4981. [PubMed: 23506476]

44. Semmler-Behnke M, Kreyling WG, Lipka J, Fertsch S, Wenk A, Takenaka S, Schmid G, Brandau W. Biodistribution of 1.4- and 18-nm Gold Particles in Rats. Small. 2008; 4:2108–2111. [PubMed: 19031432]

45. Namekawa K, Fukuda M, Matsuda M, Yagi Y, Yamamoto KI, Sakai K. Nanotechnological Characterization of Human Serum Albumin Adsorption on Wet Synthetic Polymer Dialysis Membrane Surfaces. ASAIO J. 2009; 55:236–242. [PubMed: 19357497]

46. Wu ZQ, Chen H, Liu XL, Zhang YX, Li D, Huang H. Protein Adsorption on Poly(*N*-vinylpyrrolidone)-Modified Silicon Surfaces Prepared by Surface-Initiated Atom Transfer Radical Polymerization. Langmuir. 2009; 25:2900–2906. [PubMed: 19437703]

47. Qin H, Nie SQ, Cheng C, Ran F, He C, Ma L, Yin ZH, Zhao CS. Insights into the Surface Property and Blood Compatibility of Polyethersulfone/Polyvinylpyrrolidone Composite Membranes: Toward High-Performance Hemodialyzer. Polym Adv Technol. 2014; 25:851–860.

48. Scheinin H, Knuuti J, Scheinin M. PET in Drug Discovery and Development: An Introduction. Ann Med. 1999; 31:430–431. [PubMed: 10680857]

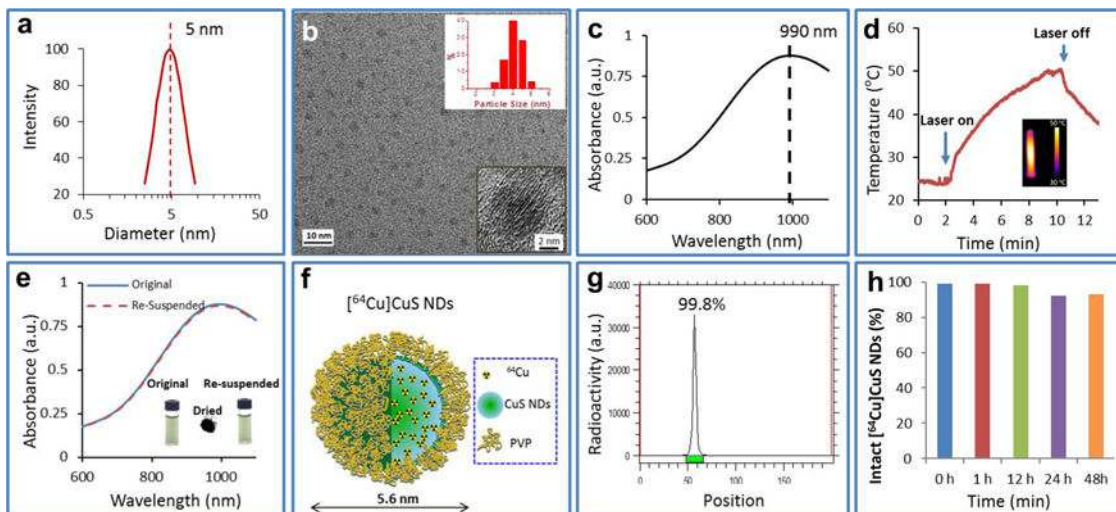49. Ametamey SM, Honer M, Schubiger PA. Molecular Imaging with PET. Chem Rev. 2008; 108:1501–1516. [PubMed: 18426240]

Figure 1.

Characterization of CuS NDs. (a) Dynamic light scattering analysis of CuS NDs showing a mean HD of 5.6 nm in aqueous solution. (b) Representative transmission electron microscopy image of CuS NDs showing a mean core size of 4.3 nm (inset). (c) UV–vis spectrum of CuS NDs in aqueous solution (50 μg/mL) showing an absorption peak in the NIR region. (d) Temperature change over time in an aqueous solution of the CuS NDs (2 OD) irradiated with an 808 nm NIR laser at 2 W/cm^2 for 10 min. Inset: Infrared thermal image of ND solution at 10 min after the start of laser irradiation. (e) UV–vis spectra of CuS NDs before ("original") and after ("resuspended") lyophilization. Inset: Photographs of ND aqueous solution before and after lyophilization and lyophilized CuS ND powder. (f) Schematic structure and (g) radiolabeling efficiency of [^{64}Cu]CuS NDs. (h) Radiolabeling stability of [^{64}Cu]CuS NDs, after incubation of [^{64}Cu]CuS NDs in phosphate buffered saline at 37°C for 2 days, more than 90% of radioactivity was associated with the NDs.
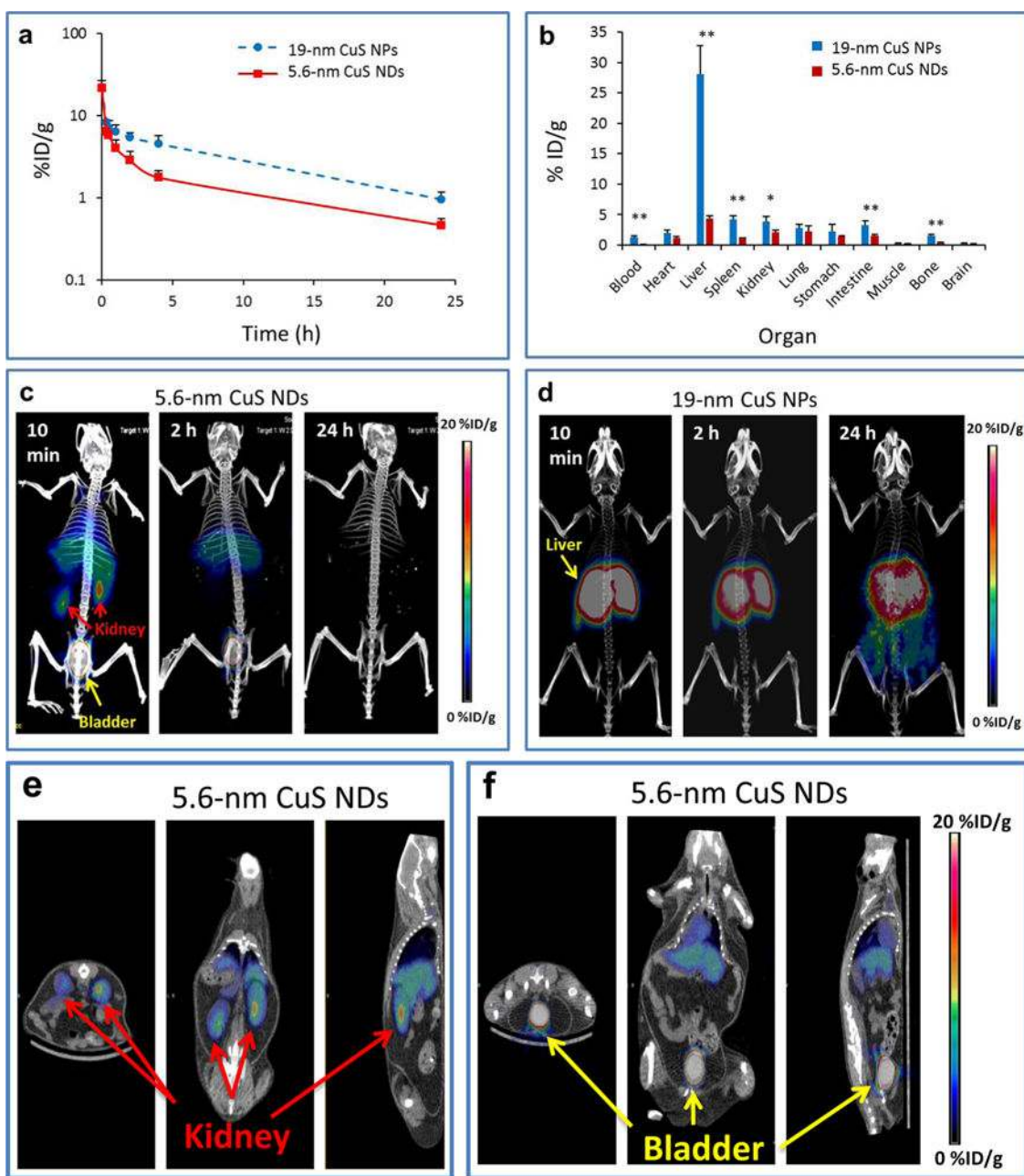
Figure 2.
Pharmacokinetics, biodistribution, and microPET/CT imaging of [^{64}Cu]CuS NDs and [^{64}Cu]CuS NPs in mice. Time–activity curves of blood (a) and biodistribution pattern at 24 h after i.v. injection (b) of the 5.6 nm [^{64}Cu]CuS NDs and the 19 nm [^{64}Cu]CuS NPs in blood ($n = 5$–6) in female Swiss mice ($n = 5$). (c,d) Representative co-registration of PET and CT (μPET/CT) maximum intensity projection images after i.v. injection of 5.6 nm [^{64}Cu]CuS NDs (c) and 19 nm [^{64}Cu]CuS NPs (d) into tumor-free Swiss mice ($n = 3$). (e,f) Representative μPET/CT 2D section images obtained at 10 min after i.v. injection of 5.6 nm [^{64}Cu]CuS NDs, showing significant accumulation of the NDs in the kidneys (e) and the

bladder (f). Left to right: transverse, coronal, and sagittal views; p values in (b) were calculated by a Student's t test (**$p < 0.001$ or *$p < 0.01$).
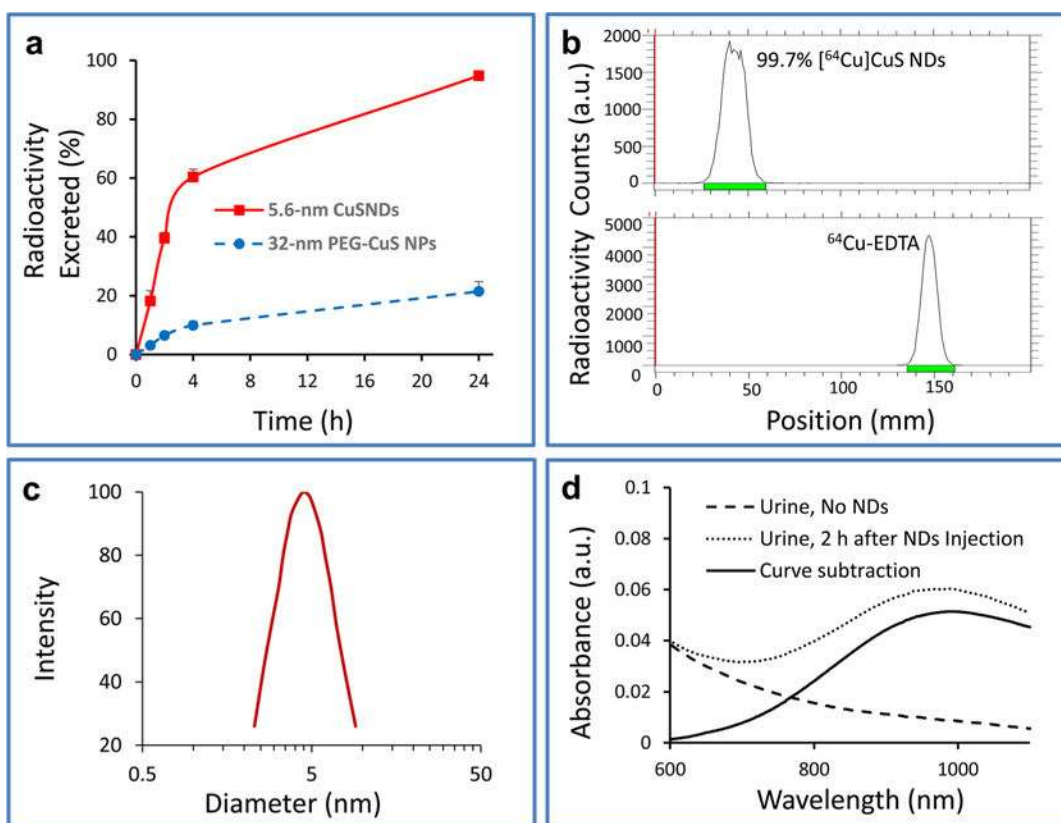
Figure 3.
Elimination of [^{64}Cu]CuS NDs from the body *via* the renal–urinary route. (a) Percentage of excreted radioactivity at different times after i.v. injection of 5.6 nm [^{64}Cu]CuS NDs, derived by subtracting the remaining radioactivity in the whole animal carcasses from the total injected radioactivity. Data are reported as mean ± standard deviation ($n = 3$). (b) Radio-TLC chromatogram of a urine sample taken from a mouse 2 h after ND injection. ^{64}Cu-EDTA solution was used as a control. (c) DLS size measurement of urine sample taken from a mouse 2 h after ND injection. (d) UV–vis spectra of a urine sample from a mouse not injected with NPs and a mouse injected with NPs.
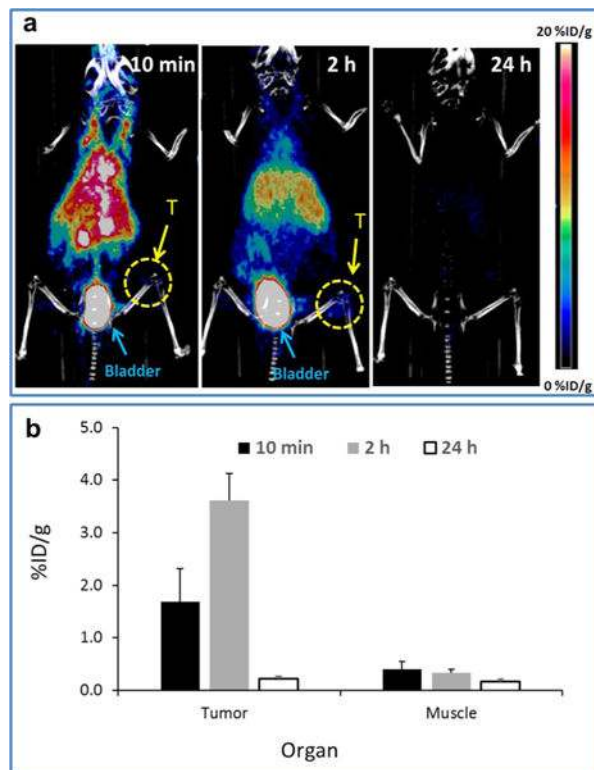
Figure 4.
MircoPET/CT imaging of CuS NDs in tumor-bearing Balb/c mice. (a) Representative co-registration of PET and CT images obtained at 10 min, 2 h, and 24 h after i.v. injection of 5.6 nm [^{64}Cu]CuS NDs into Balb/c mice bearing subcutaneous 4T1 breast tumors. Bl, bladder; T, tumor. (b) Quantitative analysis of uptake of [^{64}Cu]CuS NDs in 4T1 tumors and muscle. Data are reported as mean ± standard deviation ($n = 3$).
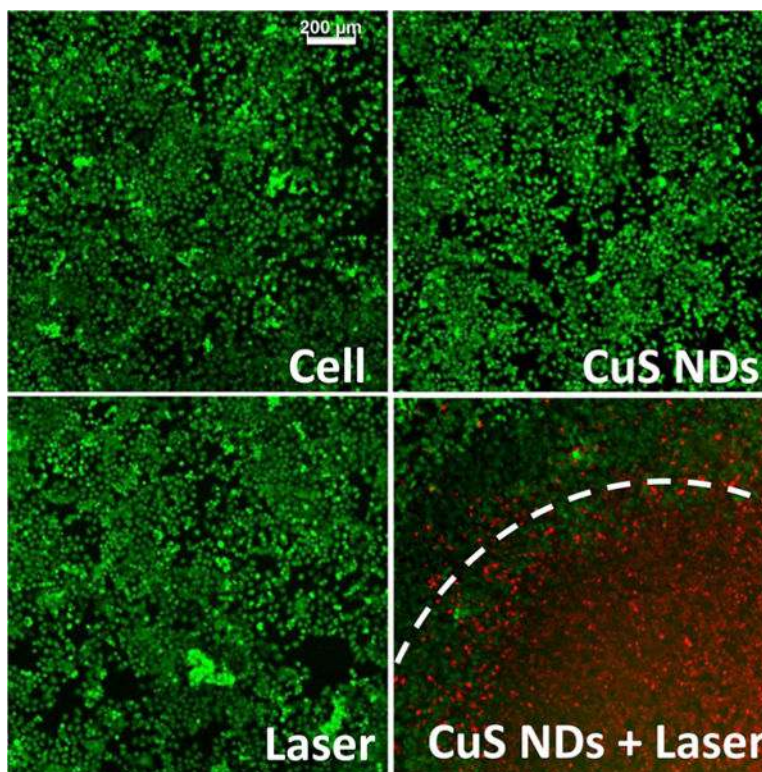
Figure 5.
Photothermal therapy of CuS NDs *in vitro. In vitro* PTA of 4T1 tumor cells. Cells were incubated with CuS NDs for 2 h, washed, and then irradiated with an 808 nm NIR laser at 2 W/cm^2 for 2 min. Viable cells were stained green with calcein-AM, and dead cells were stained red with ethidium homodimer-1. Cells inside the irradiation zone were stained intensely red, indicative of dead cells, whereas those outside the irradiation zone remained green, indicative of live cells.
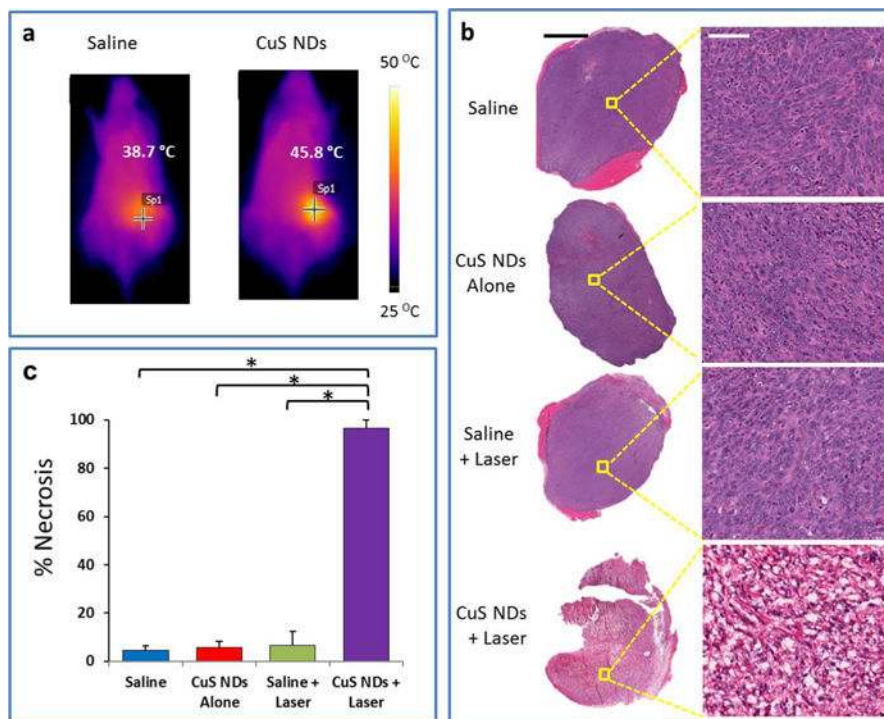
Figure 6.
Photothermal therapy of CuS NDs *in vivo*: tumor ablation. (a) Representative *in vivo* infrared thermographic images of Balb/c mice with 4T1 breast tumors exposed to an 808 nm laser at 2 W/cm^2 for 2 min beginning 2 h after i.v. injection of 5.6 nm CuS NDs (8 OD, 200 μL/mouse). Mice treated with saline and exposed to the laser under the same conditions were included as a control. (b) Histological staining (hematoxylin and eosin) of 4T1 tumors after various treatments. Treatment with 5.6 nm CuS NDs followed by 808 NIR laser (2 W/cm^2 for 2 min) induced extensive necrosis. Scale bars: left, 1 mm; right, 50 μm. (c) Quantitative analysis of the percentage of necrosis induced by various treatments. The amount of necrosis is presented as a percentage of the whole tumor area. Error bars represent standard deviations ($n = 3$). Asterisks indicate statistical significance relative to the control ($p < 0.01$).
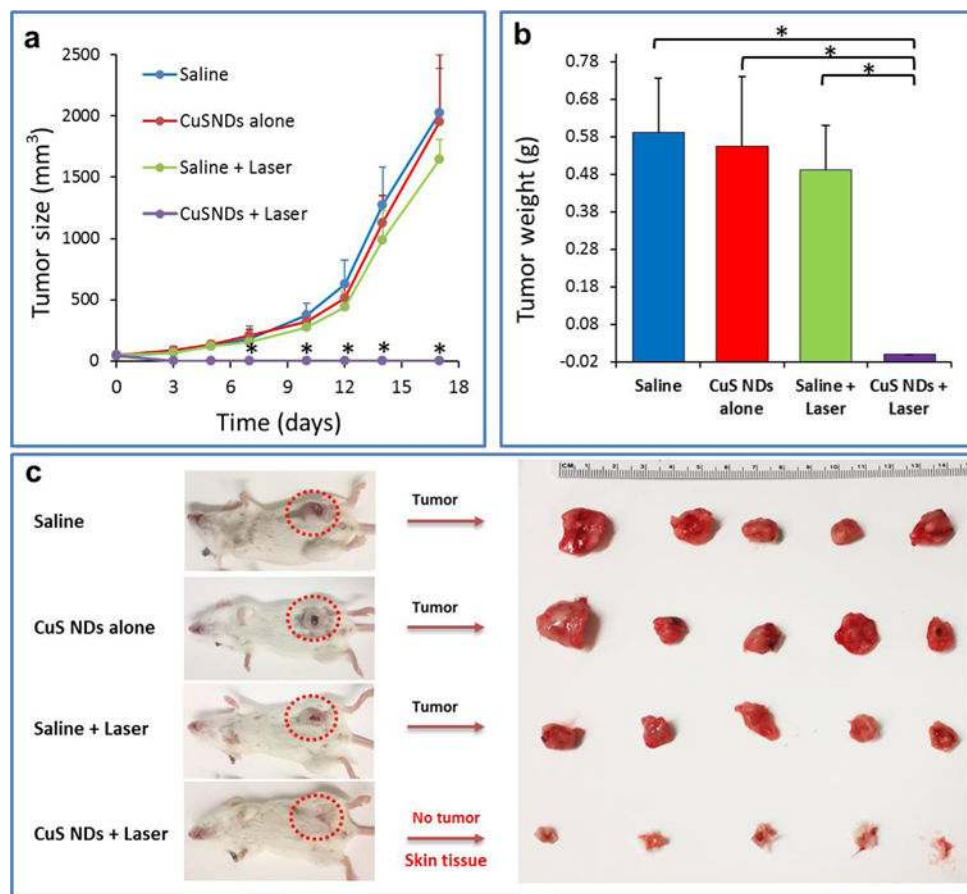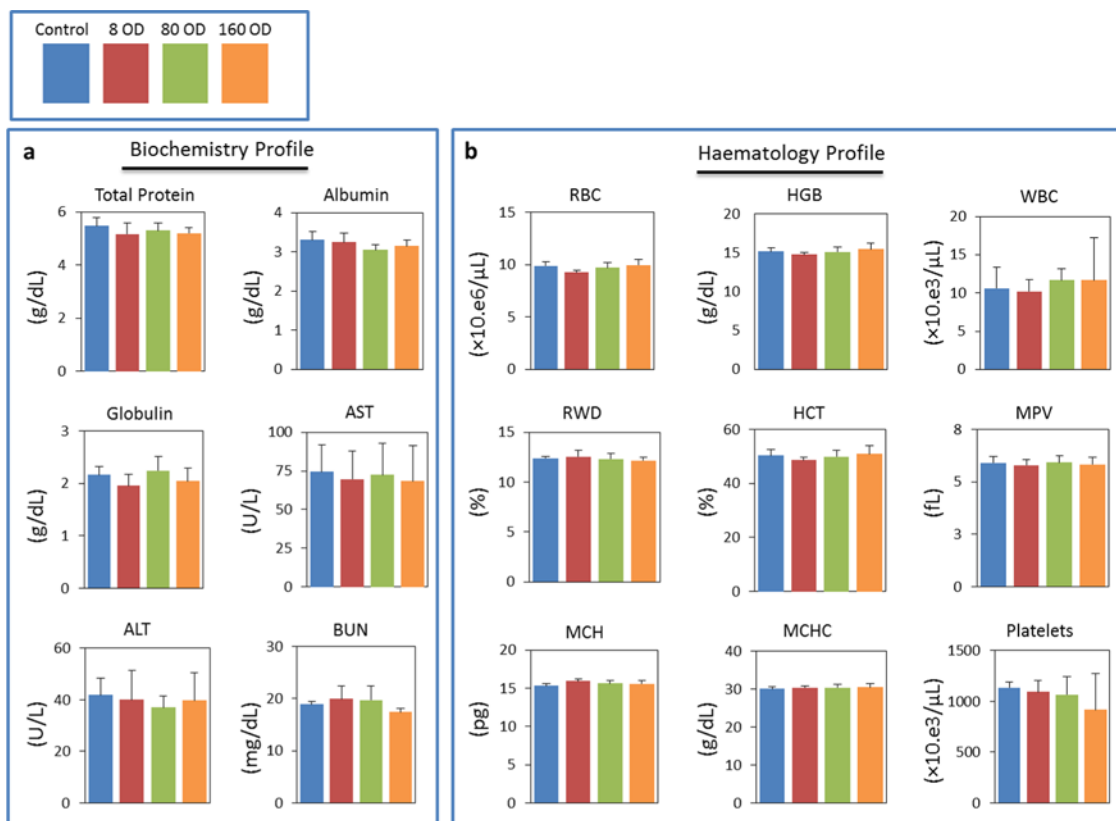
Figure 7.
Photothermal therapy of CuS NDs *in vivo*: tumor growth delay. (a) Tumor growth curves of different groups of mice after various treatments indicated. Error bars are based on standard deviation of the mean of five tumors per group. (b) Tumor weights and photos of the tumors collected from different groups of mice at the end of treatment (day 17). Note that for the CuS NDs + laser group, none of mice had tumors and only skin tissues were collected ($p <$ 0.01).

Figure 8.
Blood biochemistry (a) and hematology (b) survey. Analysis was performed on male CD1 mice 24 h after i.v. injection with either CuS NDs (200 μL/mouse, dose: 8, 80, and 160 OD) or with PBS (control). No significant changes with all tested parameters were detected. Error bars represent standard deviation from 5 to 6 independent replicates. AST, aspartate transferase; ALT, alanine transferase; BUN, blood urea nitrogen; RBC, red blood cells; HGB, hemoglobin; WBC, white blood cells; RWD, red cell distribution width; HCT, hematocrit; MPV, mean platelet volume; MCH, mean corpuscular hemoglobin; MCHC, mean corpuscular hemoglobin concentration.

TABLE 1

Pharmacokinetic Parameters for 5.6 nm [^{64}Cu]CuS NDs and 19nm [^{64}Cu] CuS NPs after Intravenous Injection into Swiss Mice[a]

HD (nm)	$t_{1/2}\alpha$ (h)	$t_{1/2}\beta$ (h)	AUC (%ID h/mL)	V_1 (mL)	V_2 (mL)	CL (mL/h)	MRT (h)
5.6	0.43 ± 0.12^b	11.69 ± 3.46^b	38.20 ± 4.22^b	8.69 ± 1.62^b	29.45 ± 11.92^b	2.65 ± 0.29^b	14.48 ± 4.86^b
19	0.11 ± 0.04	16.16 ± 0.78	134.00 ± 26.60	4.58 ± 1.07	13.06 ± 3.22	0.77 ± 0.16	22.82 ± 1.06

[a] Values are means ± standard deviations. Abbreviations: $t_{1/2}\alpha$, blood distribution half-life; $t_{1/2}\beta$, blood terminal elimination half-life; AUC, area under the blood activity–time curve; V_1, volume of distribution in center compartment; V_2, volume of distribution in the peripheral compartment; CL, total body clearance; MRT, mean residence time.

[b] Significant difference between the two types of CuS NPs with $p < 0.01$.